

Supplementary materials -for-

Determining the mechanical and decomposition properties of high energetic materials (α -RDX, β -HMX, and ε -CL-20) using a neural network potential

Mingjie Wen, Xiaoya Chang, Yabei Xu, Dongping Chen, Qingzhao Chu*

*State Key Laboratory of Explosion Science and Safety Protection, Beijing Institute of Technology,
Beijing 100081, P. R. China*

In the supplementary materials, we present:

- Fig. S1 Statistics of all sampled energy and force of RDX (a), HMX (b), and CL-20 (c) crystals in NNP training within the temperature range of 300-4000 K.
- Table S1 Computational cost of NNP-GPU, NNP-CPU, ReaxFF-CPU methods for bulk RDX systems with 168 to 168,000 atoms, bulk HMX systems with 56 to 56,000 atoms, and bulk CL-20 systems with 144 to 144,000 atoms.
- Table S2 Elastic constants of α -RDX, β -HMX, and ε -CL-20 crystals obtained from experiments and NNP simulations.
- Fig. S2 Gaseous species during the decomposition of RDX (a), HMX (b), and CL-20 (c) predicted by our previous NNP-RDX-22 model²¹. Left and right subplots represent the major and minor species, respectively.

* Corresponding author, E-mail: chuqz@bit.edu.cn (Q. Z. Chu).

1. Diversity of the sampled data on PES

To ensure the reliability of the NNP model, it is crucial to verify that the energy and force data of the training set effectively cover the sample space and ensure sufficient sampling^{1, 2}. Fig. S1 provides histograms of the energy and force distributions in the datasets of RDX, HMX, and CL-20 crystals, comprising 28,210 structures and 10,155,600 force components. Evidently, the applicability ranges of energy and force obtained from DFT calculations for the initial datasets of RDX, HMX, and CL-20 exhibit reasonable normal distributions, generating a series of accurate models. As shown in Fig. S1, the initial datasets for RDX, HMX, and CL-20 exhibit a maximum distribution (Max) of energy configurations in the range of 0.81 to 4.49 eV/atom, with energy standard deviations (Std) ranging from 0.20 to 0.71 eV/atom. Simultaneously, the maximum absolute values of forces in the initial datasets for the three crystals are distributed within the range of 43.50 to 80.27 eV/Å, with force absolute Std values ranging from 1.92 to 3.25 eV/Å. These observed results confirm that RDX, HMX, and CL-20 crystals exhibit a rich sample space within the the sampled data.

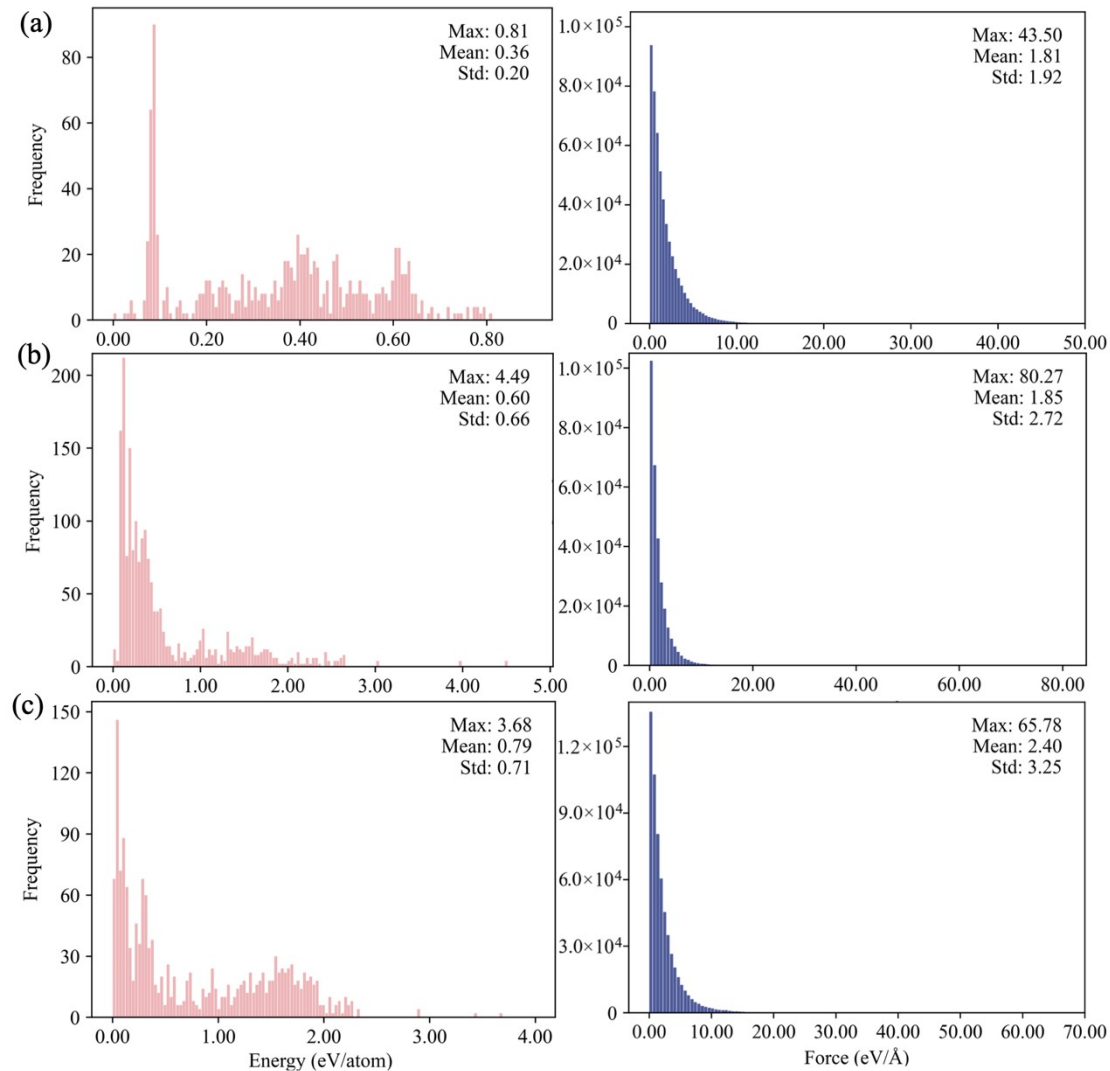


Fig. S1 Statistics of all sampled energy and force of RDX (a), HMX (b), and CL-20 (c) crystals in NNP training within the temperature range of 300-4000 K.

2. Computational efficiency of NNP and ReaxFF model

Table S1 Computational cost of NNP-GPU, NNP-CPU, ReaxFF-CPU methods for bulk RDX systems with 168 to 168,000 atoms, bulk HMX systems with 56 to 56,000 atoms, and bulk CL-20 systems with 144 to 144,000 atoms.

System	Atom numbers	ReaxFF-CPU (s/atom·step ⁻¹)	NNP-CPU (s/atom·step ⁻¹)	NNP-GPU (s/atom·step ⁻¹)
RDX	168	2.98E-03	8.33E-04	5.95E-04
	1344	1.86E-03	5.21E-04	1.93E-04
	4536	1.96E-03	5.47E-04	8.60E-05
	10752	2.04E-03	5.23E-04	4.65E-05
	21000	2.13E-03	5.24E-04	3.33E-05
	36288	2.03E-03	5.16E-04	2.81E-05
	57624	2.07E-03	5.16E-04	2.08E-05
	86016	2.02E-03	5.14E-04	2.05E-05
	122472	1.95E-03	5.21E-04	1.68E-05
	168000	1.97E-03	4.70E-04	1.48E-05
HMX	56	3.57E-03	2.14E-03	1.79E-03
	448	2.68E-03	1.23E-03	4.02E-04
	1512	2.91E-03	7.41E-04	1.59E-04
	3584	2.01E-03	6.98E-04	8.37E-05
	7000	2.12E-03	5.86E-04	5.14E-05
	12096	2.01E-03	6.07E-04	3.72E-05
	19208	1.85E-03	5.35E-04	2.81E-05
	28672	1.85E-03	5.32E-04	2.37E-05
	40824	1.95E-03	5.23E-04	1.94E-05
	56000	1.93E-03	5.43E-04	1.75E-05
CL-20	144	5.00E-03	1.11E-03	9.03E-04
	1152	2.78E-03	5.90E-04	2.08E-04
	3888	2.09E-03	5.61E-04	9.00E-05
	9216	2.06E-03	5.56E-04	7.05E-05
	18000	2.00E-03	5.58E-04	4.00E-05
	31104	1.96E-03	5.56E-04	3.05E-05
	49392	1.95E-03	5.56E-04	2.43E-05
	73728	1.94E-03	5.50E-04	2.03E-05
	104976	1.95E-03	5.44E-04	1.76E-05
	144000	1.93E-03	5.48E-04	1.56E-05

3. Computational method for elastic constant calculation using NNP model

To validate the accuracy of the trained NNP model in predicting elastic properties, we employed the DPGEN-Autotest package to perform calculations of the elastic constants for α -RDX, β -HMX, and ϵ -CL-20. The specific information about the calculations can be found in Ref. ³⁻⁶. In particular, α -RDX adopts a cubic crystal structure characterized by 9 elastic constants, while both β -HMX and ϵ -CL-20 crystals exhibit a monoclinic crystal structure, resulting in 13 elastic constants. The computed results are depicted in Fig. 6 and Table S2. Subsequent to obtaining the elastic constants, the shear modulus (G) and bulk modulus (B_0) can be derived based on the Voigt-Reuss-Hill ⁷⁻⁹ approximation model. Taking the cubic crystal system as an example:

Voigt average:

$$G_V = \frac{1}{5}[(C_{11} - C_{12}) + 3C_{44}] \quad (1)$$

$$B_V = \frac{1}{3}(C_{11} + 2C_{12}) \quad (2)$$

Reuss average:

$$G_R = \frac{5C_{44}(C_{11} - C_{12})}{3(C_{11} - C_{12}) + C_{44}} \quad (3)$$

$$B_R = \frac{1}{3}(C_{11} + 2C_{12}) \quad (4)$$

Hill average:

$$G = \frac{1}{2}(G_V + G_R) \quad (5)$$

$$B = \frac{1}{2}(B_V + B_R) \quad (6)$$

From G and B , Young's modulus (E) and Poisson's ratio (μ) can be obtained:

$$E = \frac{9BG}{3B + G} \quad (7)$$

$$\mu = \frac{3B - 2G}{2(3B + G)} \quad (8)$$

Table S2 Elastic constants of α -RDX, β -HMX, and ϵ -CL-20 crystals obtained from experiments and NNP simulations.

Elastic constants (GPa)	α -RDX	β -HMX	ϵ -CL-20
C11	38.17 (32.90) ^a , (31.70) ^b , (36.67) ^c , (25.60) ^d	30.26 (22.20) ^a , (29.30) ^e , (18.41) ^f , (20.80) ^g , (20.58) ^h	20.31 (30.10) ^a , (34.26) ⁱ , (18.89) ^j , (7.70) ^k
C22	31.00 (25.90) ^a , (26.00) ^b , (25.67) ^c , (21.30) ^d	26.48 (21.70) ^a , (25.00) ^e , (14.41) ^f , (26.90) ^g , (19.69) ^h	32.00 (28.50) ^a , (33.26) ⁱ , (18.95) ^j , (28.29) ^k
C33	27.48 (23.40) ^a , (24.70) ^b , (21.64) ^c , (19.00) ^d	23.67 (22.10) ^a , (27.50) ^e , (12.44) ^f , (18.50) ^g , (18.24) ^h	35.30 (35.00) ^a , (30.78) ⁱ , (32.16) ^j , (28.05) ^k
C44	5.46 (7.50) ^a , (6.20) ^b , (11.99) ^c , (5.38) ^d	7.54 (13.80) ^a , (13.60) ^e , (4.77) ^f , (4.20) ^g , (9.92) ^h	10.96 (5.00) ^a , (10.63) ⁱ , (8.63) ^j , (12.64) ^k
C55	3.34 (5.20) ^a , (5.20) ^b , (2.72) ^c , (4.27) ^d	6.48 (10.10) ^a , (12.80) ^e , (4.77) ^f , (6.10) ^g , (7.69) ^h	5.48 (6.50) ^a , (12.64) ⁱ , (4.24) ^j , (3.86) ^k
C66	5.37 (7.90) ^a , (8.80) ^b , (7.68) ^c , (7.27) ^d	11.90 (8.20) ^a , (13.90) ^e , (4.46) ^f , (2.50) ^g , (10.67) ^h	6.43 (8.10) ^a , (8.61) ⁱ , (3.67) ^j , (4.73) ^k
C12	7.94 (10.50) ^a , (9.40) ^b , (1.38) ^c , (8.67) ^d	13.34 (11.90) ^a , (10.60) ^e , (6.37) ^f , (4.80) ^g , (9.65) ^h	12.42 (8.20) ^a , (5.95) ⁱ , (7.33) ^j , (5.69) ^k
C13	7.66 (6.70) ^a , (3.60) ^b , (1.67) ^c , (5.72) ^d	18.90 (11.60) ^a , (13.80) ^e , (10.50) ^f , (12.50) ^g , (9.75) ^h	14.67 (7.40) ^a , (7.29) ⁱ , (4.80) ^j , (9.21) ^k
C15	-	-0.07 (0.60) ^a , (-2.10) ^e , (-1.10) ^f , (-0.50) ^g , (-0.61) ^h	2.61 (0.20) ^a , (-2.04) ⁱ , (1.29) ^j , (1.23) ^k
C23	9.76 (9.50) ^a , (7.30) ^b , (9.17) ^c , (6.40) ^d	12.71 (13.30) ^a , (16.60) ^e , (6.42) ^f , (5.80) ^g , (12.93) ^h	9.20 (2.00) ^a , (0.44) ⁱ , (1.59) ^j , (-1.22) ^k
C25	-	3.04	3.89

		(5.70) ^a , (6.20) ^c , (0.83) ^f , (-1.90) ^g , (4.89) ^h	(1.20) ^a , (3.31) ⁱ , (1.79) ^j , (1.01) ^k
C35	-	0.59	0.90
		(0.70) ^a , (1.10) ^c , (1.08) ^f , (1.90) ^g , (1.57) ^h	(1.00) ^a , (0.51) ⁱ , (0.07) ^j , (3.07) ^k
C46	-	5.11	1.23
		(8.10) ^a , (6.80) ^c , (2.75) ^f , (2.90) ^g , (4.42) ^h	(0.50) ^a , (0.62) ⁱ , (-0.66) ^j , (0.74) ^k
Bulk modulus(B_0)	16.29	18.50	16.80
	(14.95) ^a , (13.56) ^b , (11.98) ^c , (11.81) ^d	(15.20) ^a , (17.89) ^c , (9.90) ^f , (12.48) ^g , (13.42) ^h	(13.05) ^a , (13.82) ⁱ , (10.53) ^j , (8.65) ^k
Shear modulus(G)	6.76	6.65	7.30
	(7.59) ^a , (7.82) ^b , (7.83) ^c , (6.21) ^d	(6.54) ^a , (9.21) ^c , (3.67) ^f , (3.38) ^g , (6.23) ^h	(8.36) ^a , (11.65) ⁱ , (6.32) ^j , (5.68) ^k
Youngs Modulus (E)	17.81	17.82	19.13
	(19.47) ^a , (19.69) ^b , (19.29) ^c , (15.85) ^d	(17.15), ^a (23.58) ^c , (9.79) ^f , (9.29) ^g , (16.19) ^h	(20.96) ^a , (27.29) ⁱ , (15.79) ^j , (3.99) ^k
Poisson Ratio (μ)	0.32	0.34	0.31
	(0.28) ^a , (0.26) ^b , (0.23) ^c , (0.28) ^d	(0.31) ^a , (0.28) ^c , (0.34) ^f , (0.38) ^g , (0.30) ^h	(0.25) ^a , (0.17) ⁱ , (0.25) ^j , (0.23) ^k

^a The values are taken from Ref. 10; ^b Ref. 11; ^c Ref. 12; ^d Ref. 13; ^e Ref. 14; ^f Ref. 15; ^g Ref. 16; ^h Ref. 17; ⁱ Ref. 18; ^j Ref. 19; ^k Ref. 20.

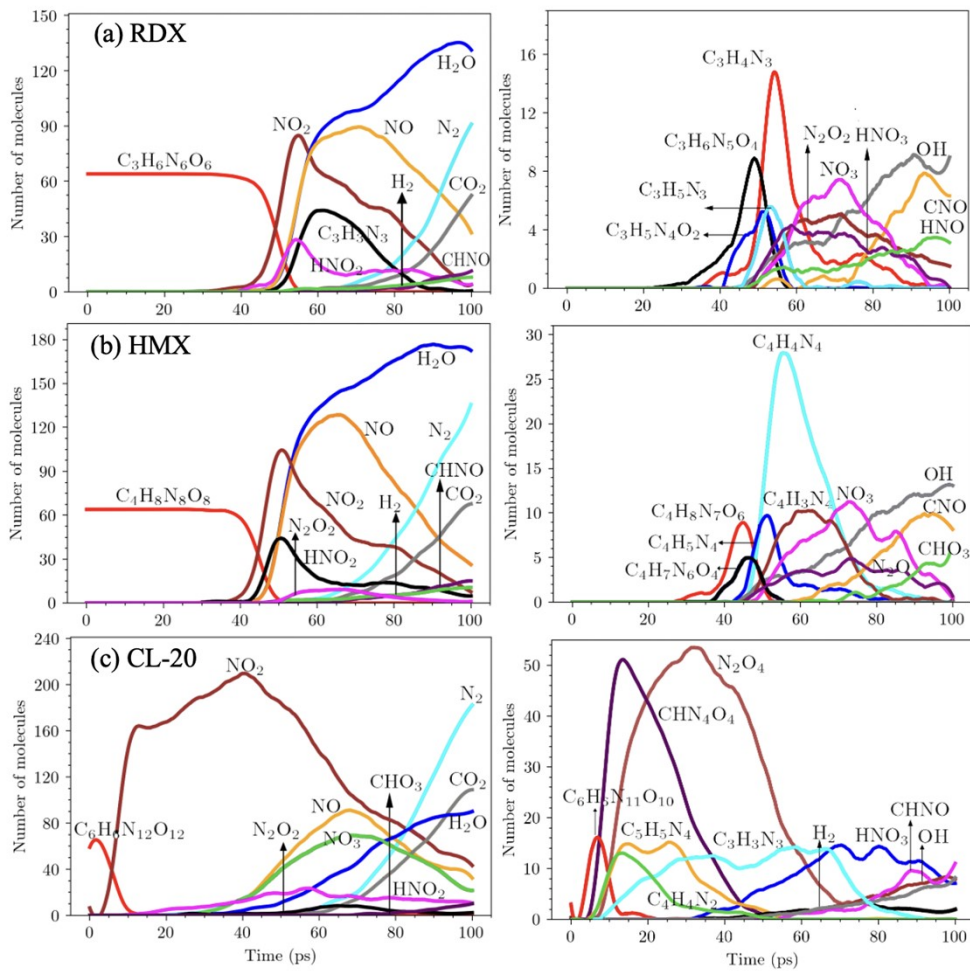


Fig. S2 Gaseous species during the decomposition of RDX (a), HMX (b), and CL-20 (c) predicted by our previous NNP-RDX-22 model²¹. Left and right subplots represent the major and minor species, respectively.

Herein, to compare the improvements observed in initial decomposition chemistry between the current model and our previous NNP model for RDX²¹, the MD simulation of the decomposition properties of RDX, HMX, and CL-20 was carried out based on NNP-RDX-22 model²¹. As shown in Fig. S2, both the previous NNP-RDX-22 model and the current NNP model exhibit good performance in the predicted decomposition processes of RDX and HMX. Specifically, in the decomposition process of RDX, the appearance of small molecular gaseous species and intermediate species shows consistent trends. For HMX, the main differences between the two models lie in the prediction of intermediate species concentrations, such as C₄H₄N₄ and C₄H₈N₇O₆. In contrast, in the presences of the NNP-RDX-22 model, CL-20 cannot stably exist and it is difficult to describe the decomposition process of CL-20, showing significant differences compared to our NNP model in this work. The above results can be attributed to the planar ring structures of RDX and HMX, while CL-20 exhibits a cage-like structure, making it difficult for the NNP-RDX-22 model to extrapolate to the prediction of thermal decomposition in cage-like energetic materials.

References:

1. J. S. Smith, R. Zubatyuk, B. Nebgen, N. Lubbers, K. Barros, A. E. Roitberg, O. Isayev and S. Tretiak, *Sci. Data*, 2020, **7**, 134.
2. P. Yoo, M. Sakano, S. Desai, M. M. Islam, P. Liao and A. Strachan, *npj Comput. Mater.*, 2021, **7**, 9.
3. <https://docs.deepmodeling.org/projects/dpgen/en/stable/autotest/property/properties/index.html>.
4. Y. Zhang, H. Wang, W. Chen, J. Zeng, L. Zhang, H. Wang and W. E, *Comput. Phys. Commun.*, 2020, **253**, 107206.
5. T. Wen, L. Zhang, H. Wang, W. E and D. J. Srolovitz, *Mater. Futures*, 2022, **1**, 022601.
6. <https://github.com/deepmodeling/dpgen/wiki>.
7. D. W. Voigt, Lehrbuch der Kristallphysik, Taubner, Leipzig, 1928.
8. A. Reuss, *ZAMM - Journal of Applied Mathematics and Mechanics / Zeitschrift für Angewandte Mathematik und Mechanik*, 1929, **9**, 49-58.
9. R. Hill, *Proceedings of the Physical Society. Section A*, 1952, **65**, 349.
10. M. J. Cawkwell, M. Zecevic, D. J. Luscher and K. J. Ramos, *Propellants, Explos. Pyrotech.*, 2022, **47**, e202100281.
11. M. Lu, Z. Zheng, G. Yu and Y. Yang, *Mater. Today Commun.*, 2023, **37**, 107375.
12. R. B. Schwarz, D. E. Hooks, J. J. Dick, J. I. Archuleta and A. R. Martinez, *J. Appl. Phys.*, 2005, **98**, 056106.
13. J. J. Haycraft, L. L. Stevens and C. J. Eckhardt, *J. Chem. Phys.*, 2006, **124**, 024712.
14. Q. Peng, Rahul, G. Wang, G. R. Liu and S. De, *Phys. Chem. Chem. Phys.*, 2014, **16**, 19972-19983.
15. L. L. Stevens and C. J. Eckhardt, *J. Chem. Phys.*, 2005, **122**, 174701.
16. J. M. Zaug, *Elastic constants of β-HMX and tantalum, equations of state of supercritical fluids and fluid mixtures and thermal transport determinations*, Proceedings of the 11th International Detonation Symposium, 1998.
17. B. Sun, J. M. Winey, Y. M. Gupta and D. E. Hooks, *J. Appl. Phys.*, 2009, **106**, 053505.
18. M. Zhong, H. Qin, Q. J. Liu, F. S. Liu and B. Tang, *Phys. Status.*, 2019, **256**, 1800440.
19. J. Tan, G. Ji, X. Chen and Z. Li, *Physica B: Condens. Matter*, 2011, **406**, 2925-2930.
20. J. J. Haycraft, *J. Chem. Phys.*, 2009, **131**, 214501.
21. Q. Chu, X. Chang, K. Ma, X. Fu and D. Chen, *Phys. Chem. Chem. Phys.*, 2022, **24**, 25885-25894.